

Design and Experimental Characterization of Mach-Zehnder Interferometer and 2-channel Microring Demultiplexer

Milana Lalovic

Abstract—This paper presents the design and implementation of integrated photonic components on a silicon-on-insulator (SOI) platform for efficient on-chip optical signal processing. Specifically, Mach-Zehnder interferometers (MZIs) and a 2-channel wavelength demultiplexer based on microring resonators will be designed, simulated, and fabricated to operate at the standard telecommunication wavelength of $\lambda = 1550$ nm. The design workflow includes waveguide modeling, layout development, and corner analysis to account for fabrication tolerances. Experimental characterization will be carried out to validate the optical performance of the fabricated devices. This work aims to demonstrate the suitability of SOI-based silicon photonics for compact and scalable photonic integrated circuits.

Index Terms—Silicon Photonics, Mach-Zehnder interferometer, ring resonators.

I. INTRODUCTION

Optical telecommunications have revolutionized long-distance data transmission by providing significantly higher bandwidth and lower latency compared to traditional electronic methods. However, translating these advantages to the chip scale remains a major challenge, particularly for efficient on-chip data communication within integrated circuits (ICs). Addressing the growing demand for faster data processing requires the seamless integration of optical and electronic components on a single chip.

Silicon photonics presents a compelling approach to this problem. Its high refractive index contrast between silicon and silicon dioxide enables strong optical confinement, making it well-suited for dense photonic integration. Furthermore, its compatibility with standard complementary metal-oxide-semiconductor (CMOS) processes facilitates cost-effective manufacturing and co-integration with electronic circuitry.

This work focuses on the design and characterization of Mach-Zehnder interferometers (MZIs) and a 2-channel wavelength demultiplexer based on microring resonators, implemented on a silicon-on-insulator (SOI) platform. Through simulation and experimental analysis, key design parameters are optimized to achieve efficient and compact optical signal processing suitable for integration in photonic integrated circuits.

II. THEORY

In SiPh, a waveguide of Silicon (Si) is surrounded with the cladding of Silicon dioxide (SiO_2), as shown in Figure 1a. Typical SOI wafers, commonly used in SiPh, consist of a silicon substrate under $2\mu\text{m}$ of oxide, also called buried

oxide (BOX). On the top of the BOX is a 220 nm layer of crystalline silicon with a layer of oxide over it. At standard telecommunication wavelength, 1550 nm, Si has a refractive index of ≈ 3.48 , while the refractive index of SiO_2 is ≈ 1.44 . [1] The high contrast between the two enables easy guidance of light through the Si. There are two types of waveguides that are commonly used in SiPh, strip and rib waveguides. The strip waveguide is a fully etched planar waveguide, as illustrated in Figure 1b, and it is usually used for routing. On the other hand, the rib waveguide is partially etched.

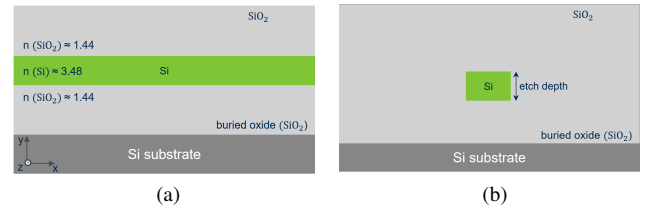


Fig. 1: (a) SOI planar slab waveguide. (b) SOI strip waveguide.

An optical mode [2] (or guided mode) refers to a specific pattern of electromagnetic fields that can propagate within an optical waveguide. It describes how light waves are confined and guided within a given structure. Modes are characterized by the distribution of electric and magnetic fields, polarization, and propagation constants. The number of allowed optical modes depends on the geometry, effective refractive index, and other properties of the waveguide. For single-mode operation of the strip waveguide at a wavelength of 1550 nm, a width of approximately 500 nm is required for a waveguide with a height of 220 nm.

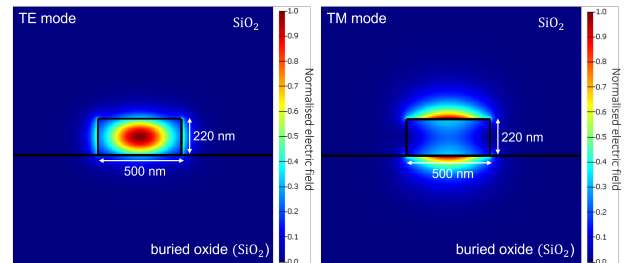


Fig. 2: Distribution of the normalised electric field of Transversal Electric and Transversal Magnetic modes in silicon strip waveguide at 1550 nm.

Two types of modes are typically found in strip and rib

waveguides: Transverse Electric (TE) and Transverse Magnetic (TM) modes. Simulation results of the normalized electric field for TE and TM modes in a strip waveguide are presented in Figure 2. It is noticeable that only the TE mode is guided in the structure of these dimensions, while the TM mode is not supported. This confirms the single-mode operation of such a waveguide.

A. Mach-Zehnder interferometer

The Mach-Zehnder Interferometer (MZI) operates by splitting an incoming light beam into two equal parts using an ideal splitter. As the light propagates through the arms of the interferometer, it accumulates phase shifts. At the point where the two beams recombine, interference occurs, and the resulting output depends on their relative phase.

The phase difference between the two arms is a critical factor for determining the nature of the interference at the output. Constructive interference occurs when the phase difference is $\Delta\phi = 2m\pi$, where m is an integer. Destructive interference, on the other hand, occurs when $\Delta\phi = (2m - 1)\pi$. Therefore, by controlling the phase difference between the two arms, the intensity of the output signal can be modulated.

In passive MZIs, the phase difference can be induced by making one arm slightly longer than the other. However, this design is fixed during fabrication and cannot be modified afterward. A schematic illustration of symmetric and asymmetric MZIs is shown in Figure 3.

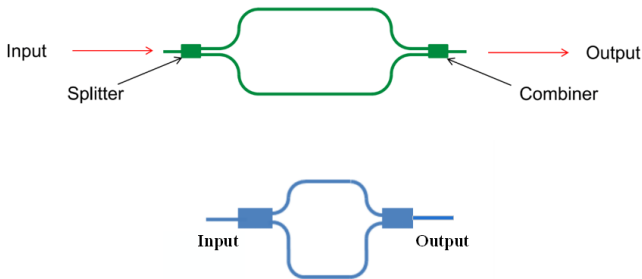


Fig. 3: Schematic representation of the symmetric (top) and asymmetric (bottom) Mach-Zehnder interferometers.

Assuming an ideal splitter and an input electric field denoted by E_{in} , the electric fields in the two arms just before recombination can be expressed as:

$$E_{out,1} = \frac{E_{in}}{\sqrt{2}} \sin(\omega t - \beta_1 L_1), \quad (1)$$

$$E_{out,2} = \frac{E_{in}}{\sqrt{2}} \sin(\omega t - \beta_2 L_2), \quad (2)$$

where $\beta = \frac{2\pi\Delta n_{eff}}{\lambda}$ is the propagation constant, λ is the wavelength of the light, and Δn_{eff} is the effective refractive index.

The total output optical power of the MZI can be expressed as:

$$P_{out} = \frac{P_{in}}{2} (1 + \cos(\Delta\phi)), \quad (3)$$

where $\Delta\phi = \beta_2 L_2 - \beta_1 L_1$ is the phase difference between the two arms. When $\Delta\phi = 0$ or a multiple of 2π , the interference is fully constructive, and the output power equals the input power (assuming negligible absorption losses in the waveguide).

B. Ring resonator

The second most common type of interferometer operates on the principle of the ring resonator. The basic structure of a ring resonator consists of a ring waveguide and a straight waveguide. The ring waveguide is a ring-shaped waveguide that is designed to trap light at certain wavelengths. The straight waveguide is placed close to the ring resonator and is used for input and output light signals.

In Figure 4, a model of the all-pass ring resonator is presented. When light is travelling through the upper waveguide, most of the wavelengths will pass through the through-port. If the resonance condition is fulfilled, the resonant wavelength will be coupled into the ring waveguide. The resonance condition is that the optical path length is equal to the product of the integer and the wavelength. More precisely, the resonance wavelength is given by the following equation:

$$\lambda_{res} = \frac{2\pi R n_{eff}}{m}. \quad (4)$$

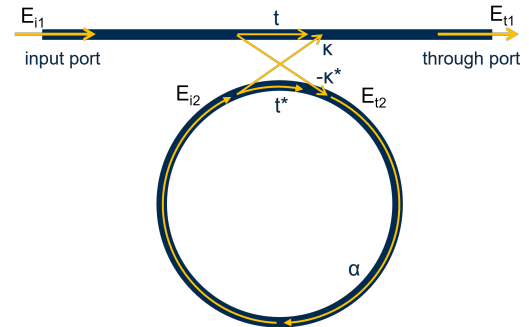


Fig. 4: Model of a ring resonator with one input port and one through port. [3]

where R is the radius of the ring, n_{eff} is the effective refractive index, and m is an integer. The principle of the light crossing from one waveguide to another is based on the evanescent field, i.e. the part of the field that is propagating outside the borders of the waveguide.

The add/drop ring resonator (Figure 5) is the configuration where the second straight waveguide is placed on the other side of the ring waveguide. This allows for partial transmission of the incident field from the first straight waveguide to the second straight waveguide.

III. MODELLING AND SIMULATION

A. Waveguide

The group refractive index (n_g) of a silicon waveguide with cross-sectional dimensions of $500 \times 220 \text{ nm}^2$ was calculated for

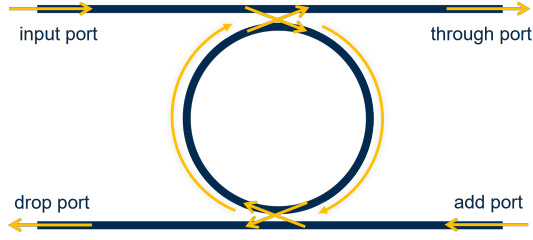


Fig. 5: Model of a ring resonator with add/drop configuration.

TE polarization at a wavelength of 1550 nm using *Lumerical* mode analysis tools. The nominal group index was found to be $n_g = 4.1964$. A corner analysis was performed to evaluate the impact of fabrication tolerances on the group index. Specifically, variations in waveguide width (470 nm to 510 nm) and height (215.3 nm to 223.1 nm) were considered.

TABLE I: Corner analysis results for TE-polarized waveguide at 1550 nm

Width (nm)	Height (nm)	n_g
470	215.3	4.2467
470	223.1	4.2556
510	215.3	4.1756
510	223.1	4.1831

From the corner analysis, the group index was found to vary between a minimum of 4.1756 and a maximum of 4.2556. This represents a possible deviation of approximately ± 0.0596 from the nominal value, reflecting the sensitivity of the waveguide dispersion to dimensional variations during fabrication.

B. Mach-Zehnder interferometer

Using Y-splitters and combiners, an asymmetric Mach-Zehnder Interferometer (MZI) was designed, as shown in Figure 3. At both the input and output ports of the interferometer, Y-junctions with a 50:50 power splitting ratio were implemented. The device was designed to operate at a central wavelength of $\lambda = 1550$ nm, and the lengths of the two interferometer arms were selected to achieve specific values of free spectral range (FSR).

To determine the necessary path length difference (ΔL) for a given FSR, the following equation was used:

$$\text{FSR} = \frac{\lambda^2}{n_g \cdot \Delta L}$$

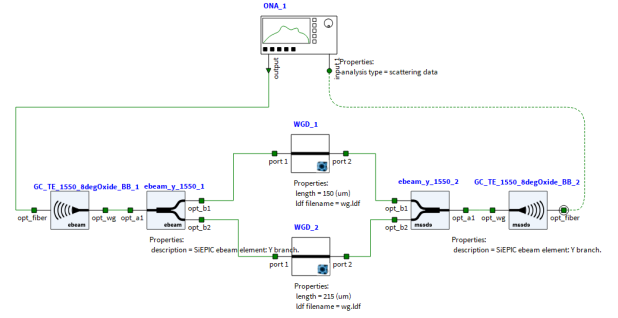
Here, $n_g = 4.1964$ is the group index of the waveguide, obtained through mode simulations using *Lumerical* software. Using this value, a path length difference of:

$$\Delta L = 65 \mu\text{m}$$

was calculated to achieve an FSR of approximately 9 nm.

To study how the length mismatch (ΔL) affects the MZI's spectral characteristics, a model was constructed in *Lumerical Interconnect*, as shown in Figure 6. The length of one of the interferometer arms was systematically varied to evaluate the resulting spectral response. As expected, the number of oscillations observed in the transmission spectrum increased

with the path length difference, demonstrating an inverse relationship between ΔL and the FSR.

Fig. 6: Mach-Zehnder Interferometer simulated in *Lumerical Interconnect*, showing Y-splitter configuration.

Simulations were performed for three different values of ΔL : 48, 65, and 130 microns. The corresponding FSRs were observed to be approximately 12, 9, and 4.5 nm, respectively. These results align with theoretical predictions and demonstrate how path length imbalance influences the interferometer's periodic transmission spectrum. Table II summarizes the simulated devices and their respective parameters.

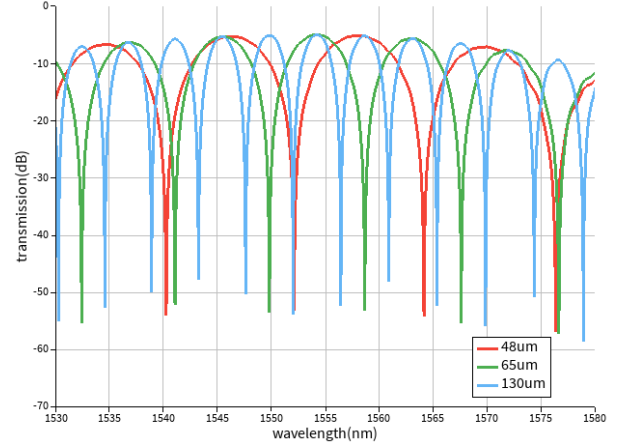
Fig. 7: Simulated transmission spectra and corresponding free spectral ranges (FSR) for $\Delta L = [130 \mu\text{m}, 65 \mu\text{m}, 48 \mu\text{m}]$.

TABLE II: MZI Device Parameters and Simulated FSR

Device	$\Delta L (\mu\text{m})$	FSR (nm)
MZI1	48	12
MZI2	65	9
MZI3	130	4.5

If the corner analysis is taken into account, variations in the waveguide width and height due to fabrication tolerances can lead to noticeable changes in the group index n_g , and consequently in the free spectral range (FSR) of the Mach-Zehnder Interferometer (MZI). For the nominal 500×220 nm waveguide operating in the TE polarization mode at $\lambda = 1550$ nm, the group index was simulated to be $n_g = 4.1964$, yielding an FSR of approximately 9.172 nm for a path length difference $\Delta L = 65 \mu\text{m}$. However, when considering corner

cases for the waveguide geometry, the group index ranged from $n_g = 4.1756$ to 4.2556 , resulting in corresponding FSRs ranging from 9.051 nm to 9.217 nm. These results highlight the sensitivity of interferometric devices to fabrication-induced variations and underscore the importance of robust design margins to ensure consistent spectral performance across fabricated chips.

TABLE III: Calculated FSR values for different waveguide geometries (TE, $\Delta L = 65 \mu\text{m}$)

Width (nm)	Height (nm)	n_g	FSR (nm)
470	215.3	4.2467	9.070
470	223.1	4.2556	9.051
510	215.3	4.1756	9.217
510	223.1	4.1831	9.201
500	220.0	4.1964	9.172

C. 2-channel demultiplexer based on ring resonator

The design and simulation of single- and dual-channel demultiplexers based on microring resonators were performed using *Lumerical Interconnect*. Figure 8 illustrates the schematic of the simulated device. A ring resonator with a radius of $R = 5 \mu\text{m}$, built from a $500 \text{ nm} \times 220 \text{ nm}$ waveguide, exhibited a simulated group index of $n_g = 4.1987$. This configuration resulted in a free spectral range (FSR) of approximately 18 nm.

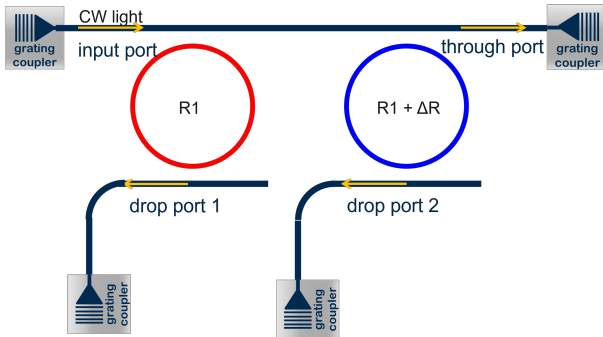


Fig. 8: Schematic of the 2-channel demultiplexer based on microring resonators.

To enable multi-channel filtering, a second ring resonator was coupled to the same bus waveguide. By carefully tuning its radius to differ slightly from the first, each ring selectively couples a different resonance wavelength. When the radii are sufficiently close, both rings maintain an FSR of 18 nm, ensuring spectral periodicity. In this configuration, resonance wavelengths corresponding to each ring are suppressed in the through port. On the other side, each ring couples its corresponding resonance wavelength to its respective drop port—Drop Port 1 for Ring 1, and Drop Port 2 for Ring 2.

Through iterative simulation, it was determined that a radius offset of $\Delta R = 0.05 \mu\text{m}$ (i.e., using $R_1 = 5.00 \mu\text{m}$ and $R_2 = 5.05 \mu\text{m}$) shifts the resonance wavelength of the second ring by approximately half the FSR (9 nm). As a result, the through port shows alternating resonance dips every 9 nm, effectively doubling the resolution, while each drop port continues to exhibit the original 18 nm FSR for its corresponding resonance.

The schematic layout of the 2-channel demultiplexer in *Lumerical Interconnect* is presented in Figure 9 and the output of the simulation is given in Figure 10.

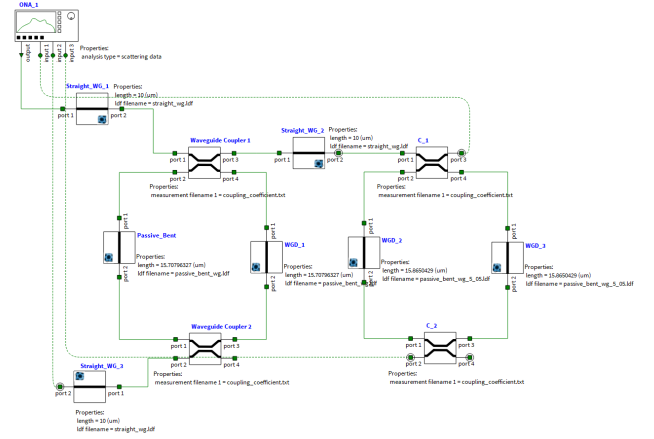


Fig. 9: Implementation of the 2-channel demultiplexer in *Lumerical Interconnect*.

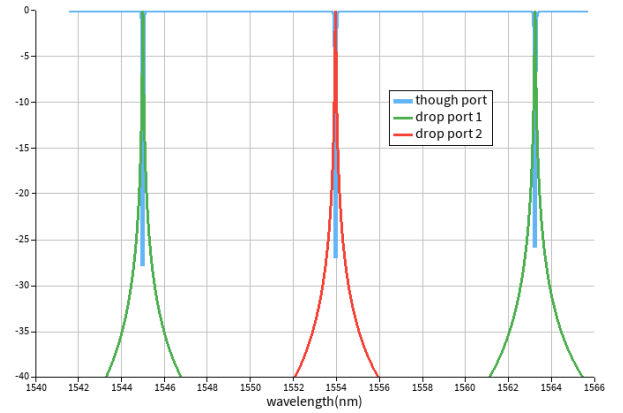


Fig. 10: Output of the *Lumerical Interconnect* simulation of the 2-channel demultiplexer.

D. Chip layout design

Following the simulation phase, the photonic chip layout was designed using *KLayout* software. Initially, a basic waveguide structure connecting two grating couplers was implemented to serve as a test structure. Two versions of this waveguide were created, with lengths of $150 \mu\text{m}$ and $200 \mu\text{m}$, respectively, to observe the effects of propagation loss over different distances.

In addition, a simple Y-splitter structure was included, with grating couplers placed at each of the two output branches. This configuration enables experimental verification of the 50:50 power splitting ratio.

Building upon these fundamental components, three asymmetric Mach-Zehnder Interferometers (MZIs) were incorporated into the layout, with path length differences ΔL of $48 \mu\text{m}$, $65 \mu\text{m}$, and $130 \mu\text{m}$, as discussed previously. To explore resonant filtering behavior, a single add/drop ring resonator with a radius of $5 \mu\text{m}$ was also added.

Furthermore, a 2-channel demultiplexer based on microring resonators, described in the previous section, was integrated into the chip layout. This structure enables wavelength-selective routing for dual-channel operation.

The complete layout of the chip, including all test structures and functional devices, is shown in Figure 11.

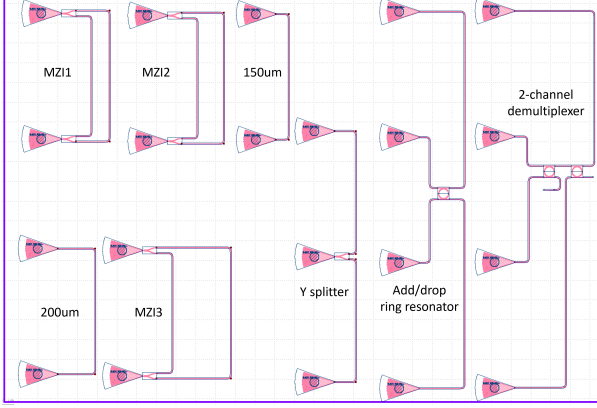


Fig. 11: Photonic chip layout designed in *KLayout*, showing waveguides, grating couplers, MZIs, ring resonators, and demultiplexer structures.

IV. FABRICATION PROCESS

Photonic devices were fabricated using the NanoSOI multi-project wafer (MPW) platform provided by *Applied Nanotools Inc.* (Edmonton, Canada; <http://www.appliednt.com/nanosoi>), which employs 100 keV direct-write electron beam lithography for high-resolution patterning. The process was carried out on 200 mm SOI wafers featuring a 220 nm crystalline silicon device layer atop a 2 µm buried oxide (BOX) layer.

Wafers were pre-diced into 25 × 25 mm substrates with backside scribe lines to facilitate post-fabrication separation into individual chips. Prior to processing, substrates were cleaned in piranha solution (3:1 H₂SO₄:H₂O₂) for 15 minutes, then rinsed with deionized water and isopropanol. A thin layer of hydrogen silsesquioxane (HSQ) resist was spin-coated and baked to eliminate residual solvents.

Electron beam lithography was performed using a JEOL JBX-8100FS system at the University of British Columbia. Proximity effect correction was applied to minimize electron backscattering, and the exposure order was optimized to reduce beam drift and increase writing efficiency. After exposure, the resist was developed in tetramethylammonium hydroxide (TMAH), and the resulting patterns were examined using optical microscopy for defects or residue.

The patterned substrates were mounted onto a 4-inch handle wafer and etched using inductively coupled plasma reactive ion etching (ICP-RIE) with chlorine gas. Etch depth was calibrated prior to processing. Remaining resist was removed using a 10:1 buffered oxide etch (BOE), and scanning electron microscopy (SEM) was used to assess pattern fidelity and sidewall quality.

To complete the process, a 2.2 µm silicon dioxide cladding layer was deposited via plasma-enhanced chemical vapor

deposition (PECVD) using tetraethyl orthosilicate (TEOS) at 300°C. Reflectometry was used throughout fabrication to monitor the thicknesses of the silicon device layer, BOX, and cladding, ensuring conformance with design specifications before final delivery.

V. EXPERIMENTAL RESULTS

Device characterization was carried out using a fully automated custom test station [4], [5], with control software developed in Python [6]. The experimental setup included an Agilent 81600B tunable laser as the input light source and Agilent 81635A optical power sensors for output detection. The wavelength was scanned from 1500 nm to 1600 nm in increments of 10 pm.

During measurements, polarization-maintaining (PM) fibres were employed to ensure stable polarization states. To couple transverse electric (TE) polarized light into the on-chip grating couplers, PM fibres were aligned accordingly [7]. For transverse magnetic (TM) mode excitation, a 90° fibre rotation was applied [7]. The light was coupled to and from the chip using a PM fibre array provided by a commercial vendor [8].

A. Waveguides

The collected spectral data from the waveguide test structures were imported into *MATLAB* for further analysis. Figure 12 shows the transmission spectra obtained from two waveguides of different lengths: 150 µm and 200 µm. Although a higher propagation loss was anticipated for the longer waveguide, both spectral curves appear very similar, with no distinct offset between them. This unexpected result is likely due to slight variations in fiber coupling efficiency during the measurements, which can introduce fluctuations that mask the relatively small difference in propagation loss over a 50 µm length difference.

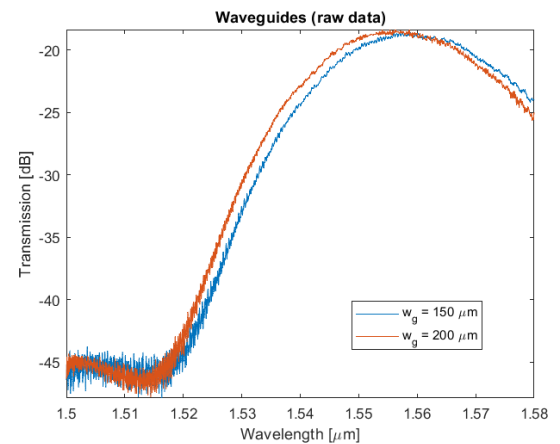


Fig. 12: Measured transmission spectra for waveguides of lengths 150 µm and 200 µm.

To accurately estimate waveguide loss using this method, it is advisable to use waveguides with significantly larger length differences, preferably exceeding 50 µm, in order to mitigate the impact of coupling variations and ensure a more reliable comparison.

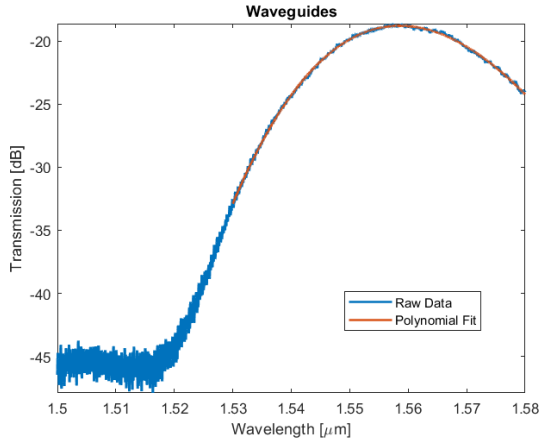


Fig. 13: Transmission spectrum of the 150 μm waveguide with 4th-order polynomial fit.

For baseline correction in subsequent analysis, only the spectrum of the 150 μm waveguide was used. This spectrum was fitted with a 4th-order polynomial in the wavelength range from 1530 nm to 1580 nm, as shown in Figure 13. The resulting polynomial fit will serve as a reference curve for normalizing the spectra of other photonic structures—such as Mach-Zehnder Interferometers (MZIs) and ring resonators—by removing the influence of the grating coupler response and waveguide transmission profile.

B. Y-Splitter

Figure 14 presents the measured transmission spectra at the two output ports of the Y-splitter. As observed, the spectra closely overlap across the entire wavelength range, indicating uniform power distribution between the two outputs. This confirms that the Y-splitter exhibits the expected 50:50 power splitting ratio with minimal imbalance. Such behavior is essential for applications like interferometers, where equal power splitting is critical to ensure constructive and destructive interference.

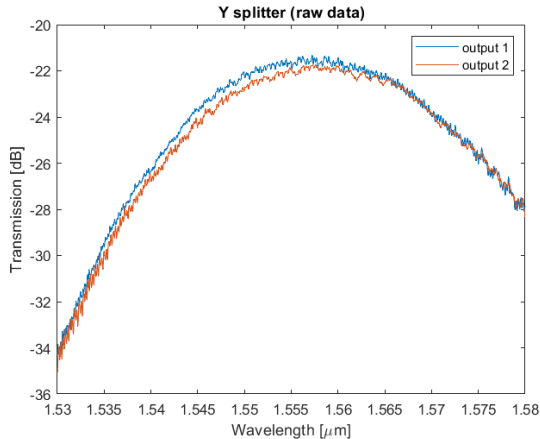


Fig. 14: Measured transmission spectra at both output ports of the Y-splitter.

C. Mach-Zehnder Interferometer

Transmission spectra were measured for all three Mach-Zehnder Interferometers (MZIs), and the resulting data was analyzed in MATLAB. Figure 15 displays the raw transmission spectrum of MZI3, which includes a baseline envelope caused by the wavelength-dependent response of the grating couplers.

To isolate the interference pattern associated with the MZI, this baseline was removed by subtracting a previously fitted polynomial corresponding to the 150 μm reference waveguide, as shown in Figure 13. This correction enables a more accurate interpretation of the spectral features that arise solely from the MZI structure. The resulting baseline-corrected spectrum is presented in Figure 16.

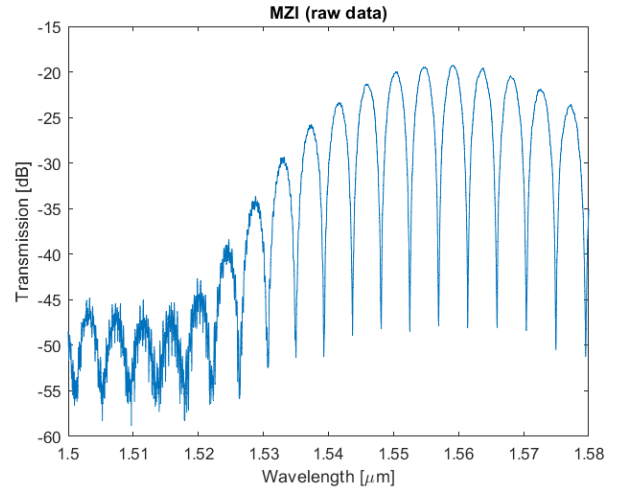


Fig. 15: Raw transmission spectrum of MZI3, showing the grating coupler-induced baseline.

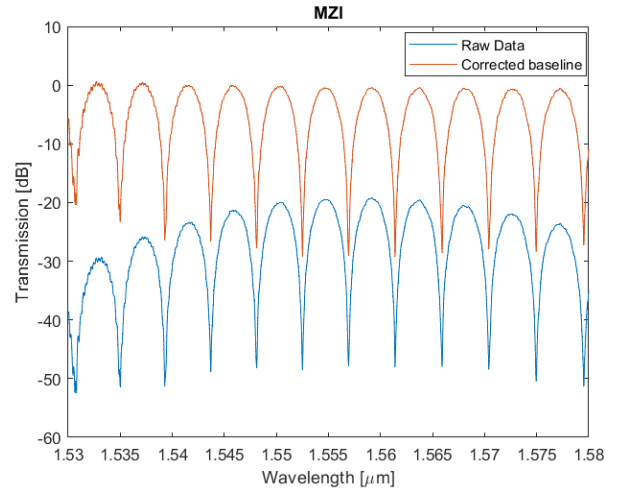


Fig. 16: Corrected transmission spectrum of MZI3 after baseline subtraction.

The same preprocessing steps were applied to the remaining two MZIs, and the corresponding spectra are shown in Figure 17. All spectra were subsequently subjected to curve fitting using MATLAB.

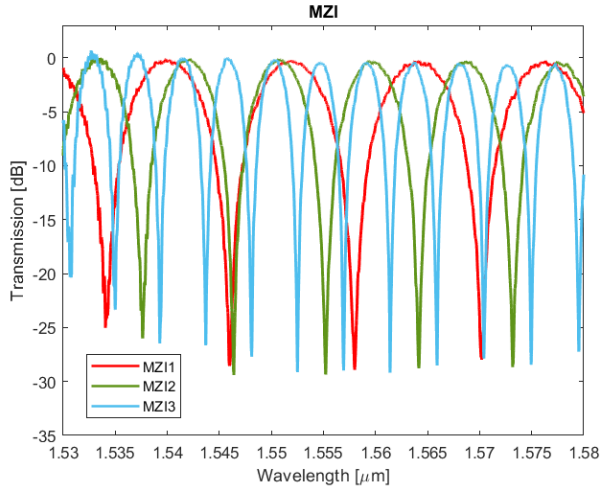


Fig. 17: Measured transmission spectra of all three MZIs after baseline correction.

To extract waveguide parameters from the measured data, a nonlinear least squares fitting algorithm was employed. This method minimizes the sum of the squared differences between the experimental data and the model. Since the transfer function is nonlinear with respect to its coefficients, a nonlinear fitting approach is necessary.

The model used for fitting is the Mach-Zehnder Interferometer transfer function, given by:

$$F = 10 \log_{10} \left(\frac{1}{4} \left| 1 + \exp \left[-i \frac{2\pi n_{\text{eff}}}{\lambda} \Delta L - \alpha \frac{\Delta L}{2} \right] \right|^2 \right) + b$$

where α represents the waveguide loss, ΔL is the path length difference between the interferometer arms (determined from the design layout), and b is an excess insertion loss term in decibels.

The wavelength-dependent effective index, n_{eff} , is modeled using a second-order Taylor expansion about a central wavelength λ_0 :

$$n_{\text{eff}} = n_1 + n_2(\lambda - \lambda_0) + n_3(\lambda - \lambda_0)^2$$

From this expression, the group index and group velocity dispersion (GVD) can be extracted. The group index is defined as:

$$n_g = n_{\text{eff}} - \lambda \frac{dn_{\text{eff}}}{d\lambda} = n_1 - n_2\lambda_0$$

while the GVD, typically reported in units of ps/nm/km, is given by:

$$D = -\frac{\lambda}{c} \frac{d^2 n}{d\lambda^2} = -\frac{\lambda}{c} \cdot 2n_3$$

Applying the fitting algorithm to the measured data for each interferometer yields the group index n_g and free spectral range (FSR) for each device. For MZI3, a group index of 4.1864 was obtained. The extracted parameters for all devices are summarized in Table IV. All extracted n_g values are in correlation with the results from the corner analysis.

TABLE IV: Extracted group indices and FSR values for all MZI structures.

Device	Group Index n_g	FSR [nm]
MZI1	4.1838	12.05
MZI2	4.1951	8.85
MZI3	4.1864	4.4

D. Ring Resonators

The transmission spectra of the 2-channel demultiplexer based on ring resonators were measured and subsequently analyzed in MATLAB. Figure 18 presents the raw transmission spectra at all three output ports of the demultiplexer. As observed, the spectra are modulated by a broad baseline envelope, which originates from the wavelength-dependent response of the grating couplers.

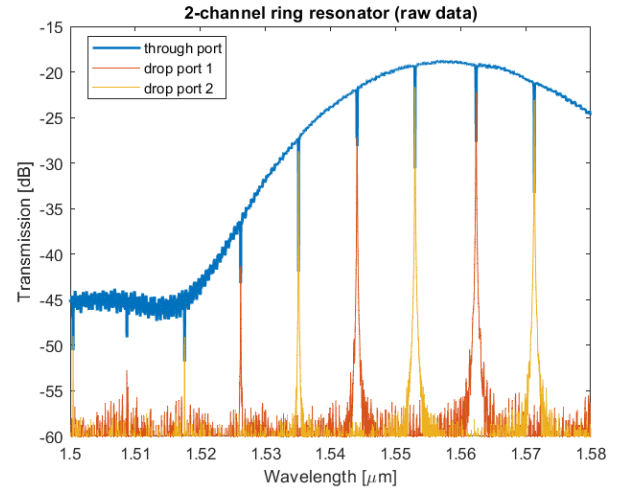


Fig. 18: Raw output spectra of the 2-channel demultiplexer based on ring resonators.

To extract the spectral characteristics of the ring resonators themselves, the baseline was corrected by subtracting the polynomial fit previously obtained from the 150 μm reference waveguide (Figure 13). The resulting corrected spectra, shown in Figure 19, allow for a clearer interpretation of the resonance behavior.

It can be seen that the through port exhibits high transmission across the wavelength range, except at the resonance wavelengths of Ring 1 and Ring 2, where the transmission dips sharply. This behavior corresponds to a free spectral range (FSR) of approximately 9 nm, indicating that the resonances of the two rings are interleaved.

In contrast, the drop port spectra exhibit low transmission overall, except at their respective resonance wavelengths, where sharp transmission peaks are observed. Both drop ports demonstrate an FSR of approximately 18 nm, consistent with the simulated design parameters. This confirms that the demultiplexer effectively separates the input spectrum into two distinct channels based on the slightly different radii of the rings.

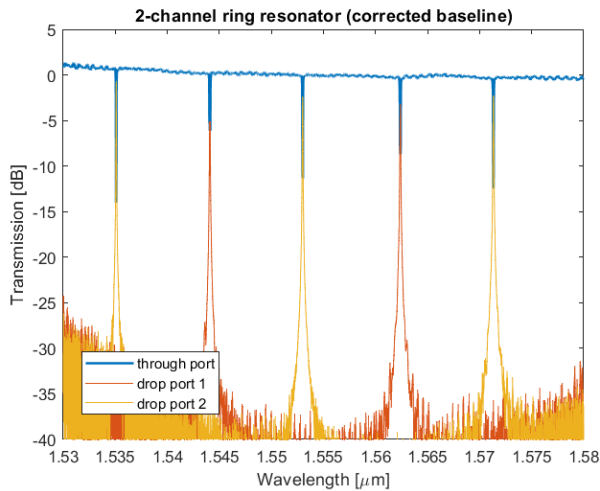


Fig. 19: Baseline-corrected transmission spectra of the 2-channel demultiplexer.

VI. CONCLUSION

This work demonstrated the successful design, simulation, and experimental validation of Mach-Zehnder interferometers and a 2-channel wavelength demultiplexer on a silicon-on-insulator platform. The fabricated MZIs exhibited free spectral ranges of 12.05 nm, 8.85 nm, and 4.4 nm, corresponding to path length differences of 48 μm , 65 μm , and 130 μm , respectively. Extracted group indices ranged from 4.1838 to 4.1951, aligning well with theoretical expectations and confirming the impact of waveguide geometry on spectral performance.

In addition, the microring-based demultiplexer achieved effective channel separation, with resonance dips spaced by approximately 9 nm and an FSR of 18 nm per ring. The spectral behavior closely matched simulation results, validating the design's ability to support wavelength-selective routing in photonic integrated circuits.

Overall, the results confirm the feasibility and robustness of SOI-based silicon photonic components for compact and scalable optical signal processing, with promising applications in high-speed data communication and integrated photonic systems.

ACKNOWLEDGMENTS

The author gratefully acknowledges the *Silicon Photonics Design, Fabrication, and Data Analysis* course (UBCx Phot1x) offered on edX, supported by the Natural Sciences and Engineering Research Council of Canada (NSERC) through the Silicon Electronic-Photonic Integrated Circuits (SiEPIC) program.

Device fabrication was carried out at Applied Nanotools Inc. Optical measurements were performed by Omid Esmaeeli at the University of British Columbia. The author also acknowledges the use of design and simulation tools provided by Lumerical Solutions, MathWorks, and KLayout.

REFERENCES

- [1] S. Pathak, "Chapter 7 - Photonics Integrated Circuits," in *Nanoelectronics*, ser. Advanced Nanomaterials. Elsevier, Jan. 2019, pp. 219–270.

- [2] A. Snyder and W. Young, "Modes of optical waveguides," *Journal of The Optical Society of America*, vol. 68, pp. 297–309, Mar. 1978.
- [3] M. Lalovic, "Radiation Effects in Silicon Photonics Optical Links," 2024, presented 16 Sep 2024. [Online]. Available: <https://cds.cern.ch/record/2910620>
- [4] L. Chrostowski and M. Hochberg, *Silicon Photonics Design: From Devices to Systems*. Cambridge University Press, 2015.
- [5] Maple Leaf Photonics, "Photonic test equipment," <http://mapleleafphotonics.com>.
- [6] M. Caverley, "Siepic probe station," <http://siepic.ubc.ca/probestation>.
- [7] Y. Wang, X. Wang, J. Flueckiger, H. Yun, W. Shi, R. Bojko, N. A. F. Jaeger, and L. Chrostowski, "Focusing sub-wavelength grating couplers with low back reflections for rapid prototyping of silicon photonic circuits," *Optics Express*, vol. 22, no. 17, pp. 20 652–20 662, 2014.
- [8] PLC Connections, "Plc connections," <http://www.plcconnections.com>.